Numerical modeling of dynamic powder compaction using the Kawakita equation of state

A. P. Mann, D. I. Pullin, M. N. Macrossan, and N. W. Page
Department of Mechanical Engineering, The University of Queensland, Queensland, Australia 4072

(Received 2 January 1991; accepted for publication 18 June 1991)

Dynamic powder compaction is analyzed using the assumption that the powder behaves, while it is being compacted, like a hydrodynamic fluid in which deviatoric stress and heat conduction effects can be ignored throughout the process. This enables techniques of computational fluid dynamics such the equilibrium flux method to be used as a modeling tool. The equation of state of the powder under compression is assumed to be a modified version of the Kawakita loading curve. Computer simulations using this model are performed for conditions matching as closely as possible with those from experiments by Page and Killen [Powder Metall. **30**, 233 (1987)]. The numerical and experimental results are compared and a surprising degree of qualitative agreement is observed.

I. INTRODUCTION

Dynamic powder compaction is a relatively new technique that uses a shock wave or a series of reflected shock waves to compress metal or ceramic powder to form a solid object. Such a shock wave system can be instigated either by an explosive charge or by impacting the powder with a high-velocity piston. When compared to quasistatic compaction (slow compression of the powder to a solid) dynamic compaction results in stronger compacts for a given average final density.[1] Another advantage of dynamic powder compaction is the greater degree of dimensional accuracy possible. It also allows interparticle bonding while the compact as a whole stays relatively cool. Hence some of the problems associated with wholesale melting of the material are avoided. Owing to the violent nature of the dynamic powder compaction process, the compacts formed show evidence of cracking and sliding motion between adjacent regions of solid compact. Understanding some of the processes involved could result in the elimination of some of these problems and hence a higher-quality final product. In order to do this the flow during the process needs to be accurately modeled. This is a task of great complexity as the flow is affected by a number of parameters including grain size, die-wall friction, amount of admixed lubricant, and shear strength of the material. In addition, powder undergoing compaction changes character, initially acting as a granular medium in which the stress-strain characteristics are governed by the laws of particle mechanics, while at higher pressures the powder solidifies so that stress is proportional to strain. Combining these and all other relevant factors into one particle-solid model is extremely difficult. Hence any attempt to model powder flow must be based on a number of simplifying assumptions.

As discussed in Gourdin[2] the application of computer modeling to powder compaction, whether quasistatic or dynamic, is still in its infancy. One of the few attempts in this area is the finite element approach investigated by Morimoto, Hayashi, and Takei[3] to study powder flow during quasistatic compaction in a die of complex geometry. This work was based on a continuum treatment of the powder material. For dynamic compaction, Berry and Williamson[4] have used computer modeling of deformation at the particle level to study local thermal and deformation features.

The present work is a computer simulation of powder flow during dynamic compaction in a die of complex geometry. It is based on a continuum treatment of the powder and explores the use of a simple inviscid fluid model to predict the global features of powder flow. This is equivalent to assuming that, to a first approximation, shear stresses and heat conduction effects are negligible. The Euler conservation equations can then be used to model the flow once an appropriate equation of state is known. The numerical technique used in the present work to solve the Euler equations is Pullin's[5] equilibrium flux method (EFM). Clearly the validity of such an approach depends on whether, for the material being compacted, shear stresses and thermal effects are small compared to the pressure effects during the compaction process. It has been shown[6] that when the pressures involved in the compaction process are significantly greater than the yield strength of the solid material then hydrodynamic fluidlike behavior will be observed. Although at the lower pressures considered presently such behavior would not dominant, the fluid assumption may nevertheless be expected to model the gross characteristics of the dynamic powder compaction process.

II. THEORY

A. Equation of state

A full treatment of the equation of state would include lattice strain and thermal components.[7] However, a much simpler approach that has been demonstrated[8] to give acceptable accuracy, at least when applied to ductile powders subjected to shocks of modest strength, is to use a quasistatic pressure-density relation. This is essentially a "cold" equation of state. Many powder loading (pressure-density) relations have been proposed[9] but that due to Kawakita has been shown to be preferable when accuracy over a wide density range is required.[10]

 0021-8979/91/063281-10$03.00

TABLE I. Kawakita constants for the three powders.

Powder	ρ_0 (kg m^{-3})	A	$B = 1/P_0$ (Pa^{-1})
Iron	2881.0	0.345	1.58×10^{-8}
Aluminum	1285.0	0.464	4.97×10^{-8}
Copper	2330.0	0.237	2.62×10^{-8}

TABLE II. Determination of modified Kawakita constant K.

Powder	a(m/s)	$(P_0/\rho_0)^{1/2}$ (m/s)	$\hat{a}$	K
Iron	4968	148.2	33.52	19.778
Aluminum	4762	125.1	38.07	24.84
Copper	3340	128.0	26.09	14.19

1. The Kawakita Model

The Kawakita equation can be written in the form

$$\hat{P}=(\hat{\rho}-1)/(1-A\hat{\rho}), \tag{1}$$

where

$$\hat{\rho}=\rho/\rho_0 \tag{2}$$

and

$$\hat{P}=P/P_0. \tag{3}$$

Here ρ is the apparent density of the powder when subjected to pressure P and ρ_0 its initial value at zero pressure. In Eq. (1), $\hat{P}$ and $\hat{\rho}$ represent the nondimensional pressure and density, respectively, of the powder while $P_0 = 1/B$ is a constant relating to the stiffness of the powder and $A = \rho_0/\rho_s$.

In terms of the fluid model used here, a Kawakita fluid is barotropic, i.e., $P=f(\hat{\rho})$ only. Differentiating the equation yields an expression for the nondimensional sound speed $\hat{a}$, that is,

$$\hat{a}=\left(\frac{\partial\hat{P}}{\partial\hat{\rho}}\right)^{1/2}=\left(\frac{1-A}{(1-A\hat{\rho})^2}\right)^{1/2}. \tag{4}$$

The sound speed in SI units a may be determined from the nondimensional sound speed using a dimensionalizing factor as follows:

$$a=\hat{a}(P_0/\rho_0)^{1/2}.$$

For comparison with the experimental flow results obtained by Page and Killen[11] the same three materials, iron, aluminum, and copper, were studied in this work. The values of the constants used in the Kawakita equation for these metals are shown in Table I.

Inspection of Eqs. (1) and (4) reveals that as $\hat{\rho}$ tends towards its asymptotic value of $1/A$ both the pressure and the sound speed are infinite. An infinite sound speed implies that the compacted material is infinitely stiff, a physically unrealistic assumption and one that is very difficult to handle numerically. A simple computational procedure to eliminate this singularity in the Kawakita equation is to adopt a modified form given by

$$\hat{P}=(\hat{\rho}-1)/R, \tag{5}$$

where

$$R=(1/2K)\ln\{2\cosh[K(A\hat{\rho}-1)]\}-\tfrac{1}{2}(A\hat{\rho}-1), \tag{6}$$

and where K is a dimensionless constant to be determined. Again $\hat{a}$ can be obtained via differentiation:

$$\hat{a}=\left(\frac{\partial\hat{P}}{\partial\hat{\rho}}\right)^{1/2}=\left(\frac{1}{R}-\frac{(\hat{\rho}-1)}{R^2}\frac{\partial R}{\partial\hat{\rho}}\right)^{1/2}, \tag{7}$$

where

$$\frac{\partial R}{\partial\hat{\rho}}=\frac{A}{2}\{\tanh[K(A\hat{\rho}-1)]-1\}. \tag{8}$$

When K is large and $\hat{\rho}$ is small the value of R tends to $1-A\hat{\rho}$, its value for the unmodified Kawakita equation. When $\hat{\rho}=1/A$ the nondimensional pressure and sound speed are given by

$$\hat{P}=2K(A-1)/A\ln 2, \tag{9}$$

$$\hat{a}=\{[2K/(\ln 2)^2][\ln 2+K(1-A)]\}^{1/2}, \tag{10}$$

which are never infinite if K remains finite. It can also be seen that as $\hat{\rho}$ gets large, the value of $\hat{P}$ will tend towards infinity. However there are no singular points. The value of K used in the modified Kawakita equation of state was chosen so that the value of nondimensional sound speed at $\hat{\rho}=1/A$ [eq. (10)] is equal to that in the solid material as shown in Table II. Using these K values, the modified Kawakita equation can be used for densities ranging from $\hat{\rho}=1$ up to $1/A$ without any singularity problems. The accuracy of the Kawakita model up to near-theoretical density has been demonstrated previously.[10] The density range of interest in this simulation is up to 90% theoretical. As both the Kawakita and modified Kawakita equations predict identical pressures for this density range then the modified equation must also be valid.

B. The equilibrium flux method

EFM is a finite volume numerical method for the solution of the continuum Euler equations. It may be derived from the Boltzmann equation of kinetic theory which, in the presence of a "body force" $\mathbf{F}(\mathbf{r},t)$ acting on all the molecules of a gas, is

$$\frac{\partial}{\partial t}(nf)+\mathbf{u}\cdot\nabla(nf)+\mathbf{F}\cdot\frac{\partial}{\partial\mathbf{u}}(nf)=\left(\frac{\partial}{\partial t}(nf)\right)_{\text{coll}}, \tag{11}$$

where n is the number density of the molecules of the gas, $f(\mathbf{u}, \mathbf{r}, t)$ is the molecular velocity distribution function, $\mathbf{u}$ is the molecular velocity, and $\mathbf{r}$ is the position. The right-hand side of Eq. (11) is the collision operator.[12] We note that in the EFM method, the "molecules" play only a conceptual role in providing a mechanism for the analytical derivation of the flux expressions that are used in the actual computations. Previous work with EFM has dealt with a perfect gas equation of state only. Presently the

effect of fluid with a barotropic equation of state of the form $P=f(\rho)$ is simulated by specifying a fictitious force $\mathbf{F}$ which acts on all the "molecules" given by

$$\mathbf{F}=\frac{1}{\rho}\nabla\left(\rho\frac{\partial P}{\partial\rho}-P\right). \tag{12}$$

The computational flowfield is divided into a number of cells or finite volumes V_j, and conservation equations can be derived by first multiplying Eq. (11) by a general molecular quantity $\mathbf{Q}$ and then integrating over all V_j and all $\mathbf{u}$. The resulting term on the right-hand side vanishes.[12] Applying the divergence theorem to the second and third terms on the left-hand side gives

$$\frac{\partial}{\partial t}\int_{V_j}\mathbf{U}\,dV+\int_S\mathbf{G}\,dS=\mathbf{0}, \tag{13}$$

where the conserved quantities (per unit volume) in each cell are

$$\mathbf{U}=\int_{-\infty}^{\infty}n\mathbf{Q}f\,d\mathbf{u} \tag{14}$$

and the outward flux of conserved quantities across dS is

$$\mathbf{G}=\int_{-\infty}^{\infty}\left[n\mathbf{Q}f\mathbf{u}\cdot\hat{\mathbf{n}}-\left(\rho\frac{\partial P}{\partial\rho}-P\right)\frac{1}{\rho}\frac{\partial\mathbf{Q}}{\partial\mathbf{u}}(nf)\right]d\mathbf{u}, \tag{15}$$

where $\hat{\mathbf{n}}$ is the outward unit normal to the surface element dS. Equation (13) can be integrated forward in time for each cell. Explicit Euler time stepping,

$$\left(\int_{V_j}\mathbf{U}\,dV\right)_{t+\Delta t}=\left(\int_{V_j}\mathbf{U}\,dV\right)_t-\Delta t\left(\int_S\mathbf{G}\,dS\right)_t, \tag{16}$$

has been used. For a barotropic equation of state only $\mathbf{Q}=m$ (the molecular mass) and $\mathbf{Q}=m\mathbf{u}$ (the molecular momentum) need be considered. Then the components of $\mathbf{U}$ are $(\rho,\rho\bar{\mathbf{u}})$ where $\rho=nm$ and $\bar{\mathbf{u}}=\int f\mathbf{u}\,d\mathbf{u}$ is the macroscopic fluid velocity.

To derive the flux in Eq. (15) it is assumed[5] that f in each cell is given by the local Maxwell–Boltzmann equilibrium distribution, that is, that

$$f=f_0(\mathbf{u})=(\beta^3/\pi^{3/2})\exp[-\beta^2(\mathbf{u}-\bar{\mathbf{u}})^2], \tag{17}$$

where $\beta=[2(\partial P/\partial\rho)]^{-1/2}$. With this f the flux expression of Eq. (15) contains no viscous terms and it can be shown by the use of elementary vector identities that Eq. (13) then reduces to the Euler equations for a fluid for which the pressure is given by the expression for P that appears in Eq. (15).

For a two-dimensional flowfield let $\hat{\mathbf{p}}$ form with $\hat{\mathbf{n}}$ an orthogonal set of axes and let the components of $\mathbf{u}$ along these axes be (u_n, u_p). Let $+$ and $-$ refer to the interior and exterior of V_j, respectively. By the assumption of local equilibrium the distribution function of the molecules crossing the surface S is given by

$$n_sf_s=\begin{cases}n^+f_0^+, & u_n>0,\\ n^-f_0^-, & u_n<0\end{cases}. \tag{18}$$

By putting the distribution (18) into Eq. (15) the flux can be split to give

$$\mathbf{G}=\mathbf{G}^+ +\mathbf{G}^-, \tag{19a}$$

where

$$\mathbf{G}^+=\int_{-\infty}^{\infty}\int_0^{\infty}n^+\mathbf{Q}f_0^+u_n\,du_n\,du_p, \tag{19b}$$

$$\mathbf{G}^-=\int_{-\infty}^{\infty}\int_{-\infty}^{0}n^-\mathbf{Q}f_0^-u_n\,du_n\,du_p. \tag{19c}$$

The integration in Eq. (19) can be performed analytically giving

$$\mathbf{G}^{\pm}=\begin{cases}W^{\pm}(\rho\bar{u}_n)\pm D^{\pm}(\rho/\beta)^{\pm},\\ W^{\pm}(\rho\bar{u}_n\bar{u}_n+P)^{\pm}\pm D^{\pm}(\bar{u}_n\rho/\beta)^{\pm},\\ W^{\pm}(\rho\bar{u}_n\bar{u}_p)^{\pm}\pm D^{\pm}(\bar{u}_p\rho/\beta)^{\pm},\end{cases} \tag{20a}$$

where

$$W^{\pm}=[1\pm\mathrm{erf}(s_n)]/2, \tag{20b}$$

$$D^{\pm}=\exp[-(s_n^{\pm})^2]/(2\pi^{1/2}), \tag{20c}$$

$$s_n^{\pm}=\bar{u}_n^{\pm}\beta^{\pm}, \tag{20d}$$

and P is given by the modified Kawakita equation of state [Eq. (9)].

For an axisymmetric flowfield the radial component of momentum in each cell must be altered at the end of each time step by an additional amount

$$P(V_j/r)\Delta t, \tag{21}$$

where r is the radial coordinate of the cell. This accounts for the net flux of radial momentum transported into the cell in the azimuthal direction. At a solid surface the net mass and tangential component of momentum fluxes across the surface are zero while the net flux of momentum in the $\hat{\mathbf{n}}$ direction is just twice the outward normal flux $\mathbf{G}^+$. When the fluxes $\mathbf{G}$ are evaluated at cell centroids either side of the interface S the method is first-order accurate in space. EFM can be made second-order accurate in space[13] by allowing for linear variations of flow properties within cells and using the minmod gradient limiter.[14] The stability condition for first- and second-order EFM is the same as that for any Euler integration of explicit type which is that the CFL number defined as

$$\mathrm{CFL}=\frac{(|\mathbf{u}|+|a|)\Delta t}{\Delta x}, \tag{22}$$

where Δx is a characteristic cell dimension, is less than unity for each cell.

III. RESULTS

A. One-dimensional test problem

As a test of the method first- and second-order versions of EFM were used to model the simple shock reflection system shown in Fig. 1. The working fluid was iron powder

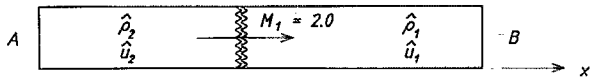

FIG. 1. One-dimensional shock reflection system. Modified Kawakita equation of state: $A=0.345$, $K=19.778$.

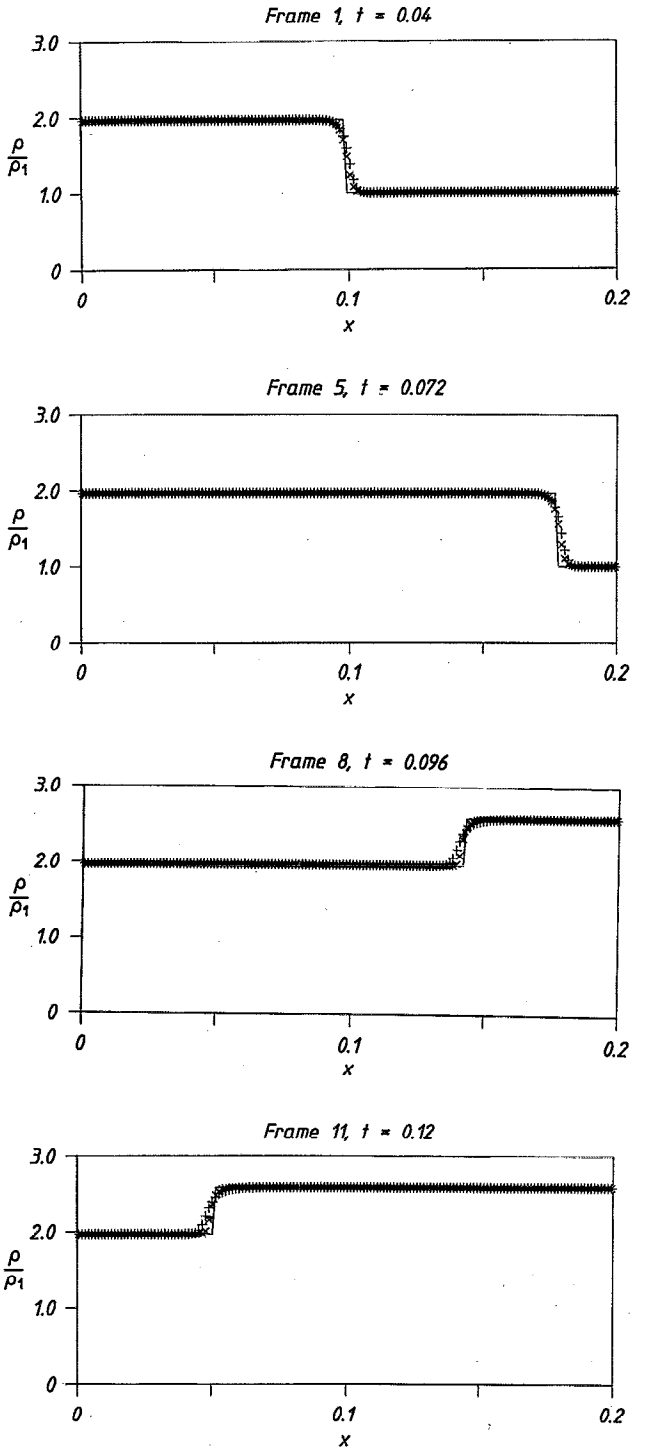

FIG. 2. Time sequence of $\hat{\rho}$ vs x plots for one-dimensional shock reflection system. +: first order; ×: second order; —: theoretical.

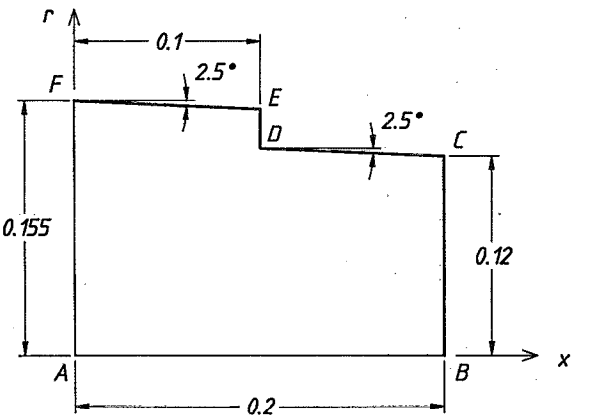

FIG. 3. Die semi-cross-section.

with a pressure density relationship given by the modified Kawakita loading curve. In Fig. 1 a shock with a Mach number of 2.0 is propagating in the positive x direction from a freestream boundary at A to a specularly reflecting surface at B. The length of the flowfield has been arbitrarily chosen to be 0.2 units and 160 internal cells are used. Such a geometry can be used to represent powder flow in a perfectly cylindrical die. Preshock conditions of $\hat{\rho}_1 = 1.0$ and $\hat{\mathbf{u}}_1 = 0.0$ were set in the internal cells and postshock conditions of $\hat{\rho}_2 = 1.966$ and $\hat{\mathbf{u}}_2 = 1.215$ were set in the freestream boundary cells in order to instigate the propagation of an $M=2.0$ shock. Snapshots of the flow were taken at 11 later times. Figure 2 shows the results obtained using first- and second-order EFM at time frames at $t=0.04$, 0.072, 0.096, and 0.12. These are compared with a theoretical solution obtained using the Rankine Hugoniot relations for a fluid with an equation of state given by Eqs. (9) and (10).

Figure 2 shows that EFM accurately predicts the speeds of the incident and reflected shocks as well as the density behind the reflected shock. Both the incident and reflected shocks, instead of being step functions, are spread over a number of cells. This "shock smearing" is characteristic of shock capturing methods such as EFM. This smearing is smaller for the second-order method.

B. Two-dimensional flow in an axisymmetric die

The code used to obtain the one-dimensional results was modified to handle the two-dimensional axisymmetric geometry used in the experiments of Page and Killen.[11] In these experiments, comparisons were made between compacts made using quasistatic and dynamic methods, the latter involving powder processing by a primary shock followed by a shock reflected from the powder support. The compacts were compared on the basis of hardness distribution and powder displacement. Powder displacement measurements involved interspersing the powder to be compacted with layers of marker powder. After the compaction process the product would be sectioned. The re-

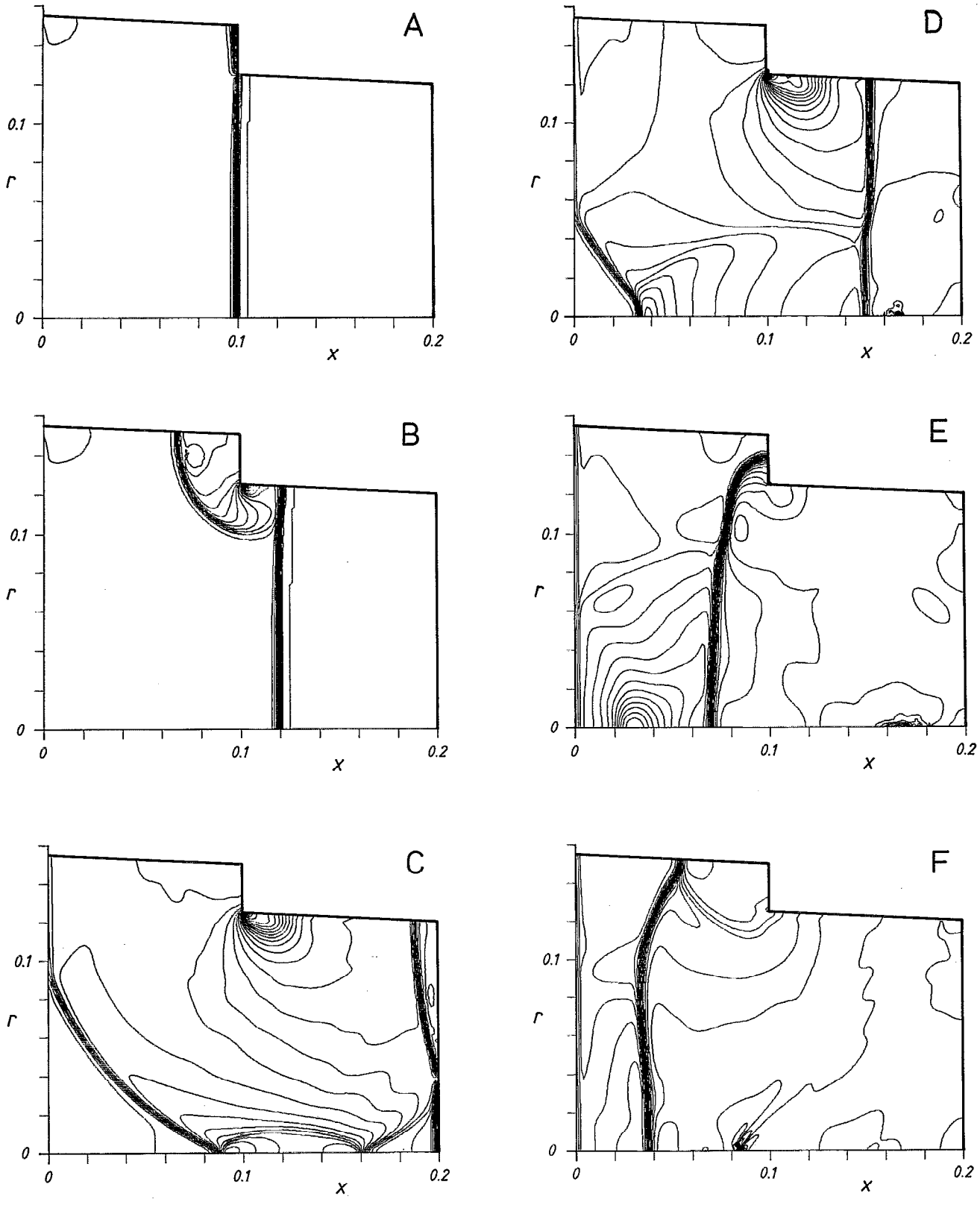

FIG. 4. Time sequence of density contours: (a) t=0.04, (b) t=0.048, (c) t=0.08, (d) t=0.088, (e) t=0.104, (f) t=0.112.

sulting positions of the marker powder layers give an indication of the history of the powder flow.

For the purposes of the EFM modeling of the same compaction geometry, the semi-cross-section of the die was proportioned as in Fig. 3. The x axis is the axis of symmetry and the r axis is in the radial direction. The side AF is a freestream boundary whereas sides BC, CD, DE, and EF are represented as specularly reflecting surfaces. Side AB is the axis of the die. In the earlier experiments, AF was 12.3 mm in physical units.

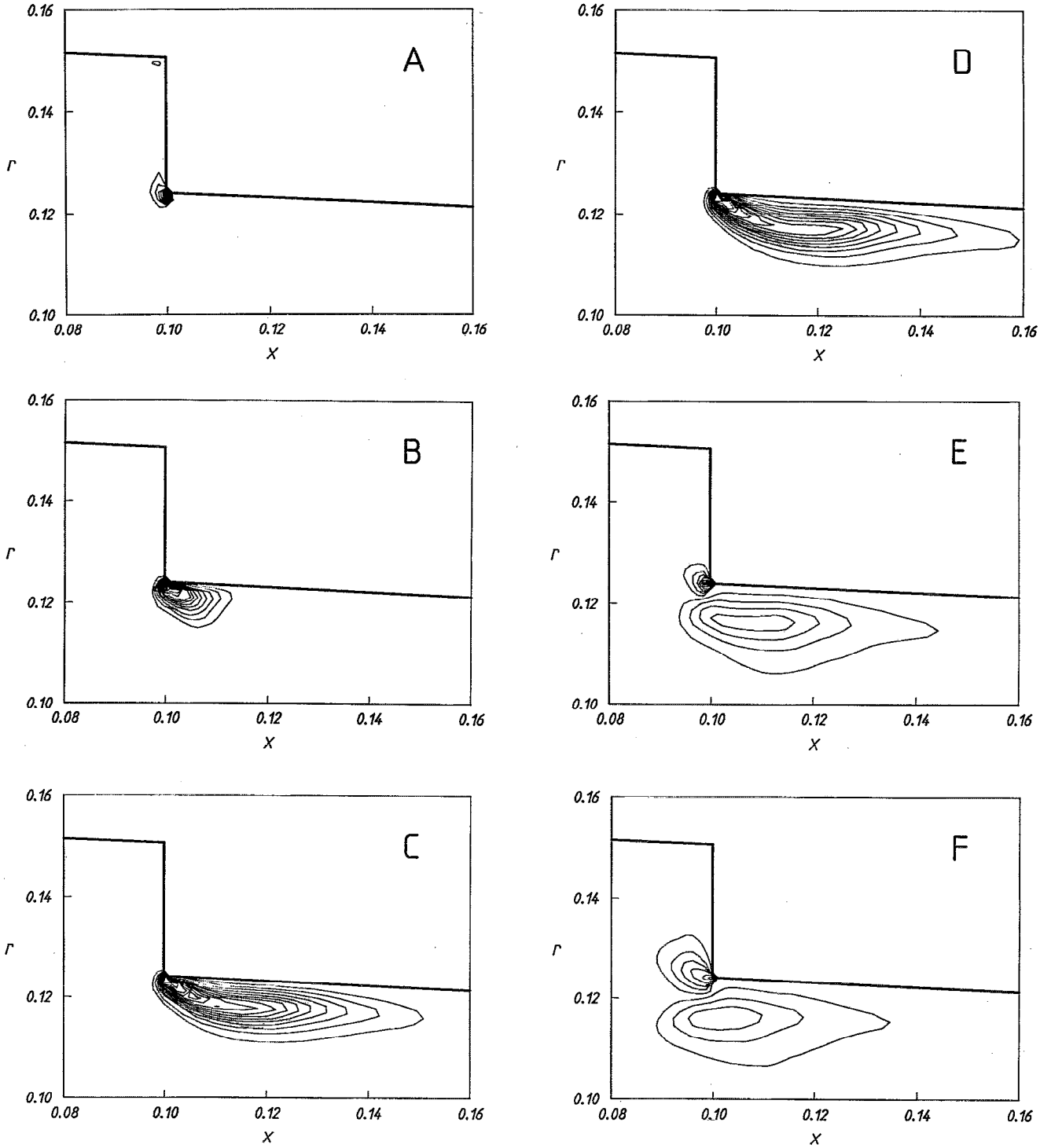

FIG. 5. Time sequence of vorticity contours in the region of the step (times as for density). Modified Kawakita equation of state: $A=0.345$, $K=19.778$.

The flowfield was initialized as for the one-dimensional case by setting the nondimensional density $\hat{\rho}$ equal to unity and the nondimensional velocity $\hat{u}$ equal to zero in the internal cells. The Mach number of the incident shock was determined from the experimental pressures and from this Mach number the nondimensional postshock density and velocity can be obtained. Figures 4, 5, and 6 show time frame sequences of the calculated density, vorticity, and maximum shear strain rate, respectively, for the case of iron powder where the initial shock Mach number was 2.0. The grid resolution used was 160 cells in the x direction and 116 cells in the radial direction.

1. Density distribution

Figure 4 shows the time frame sequence of density contours. The darker regions of the plot represent areas of rapid density changes associated with shock waves. It can

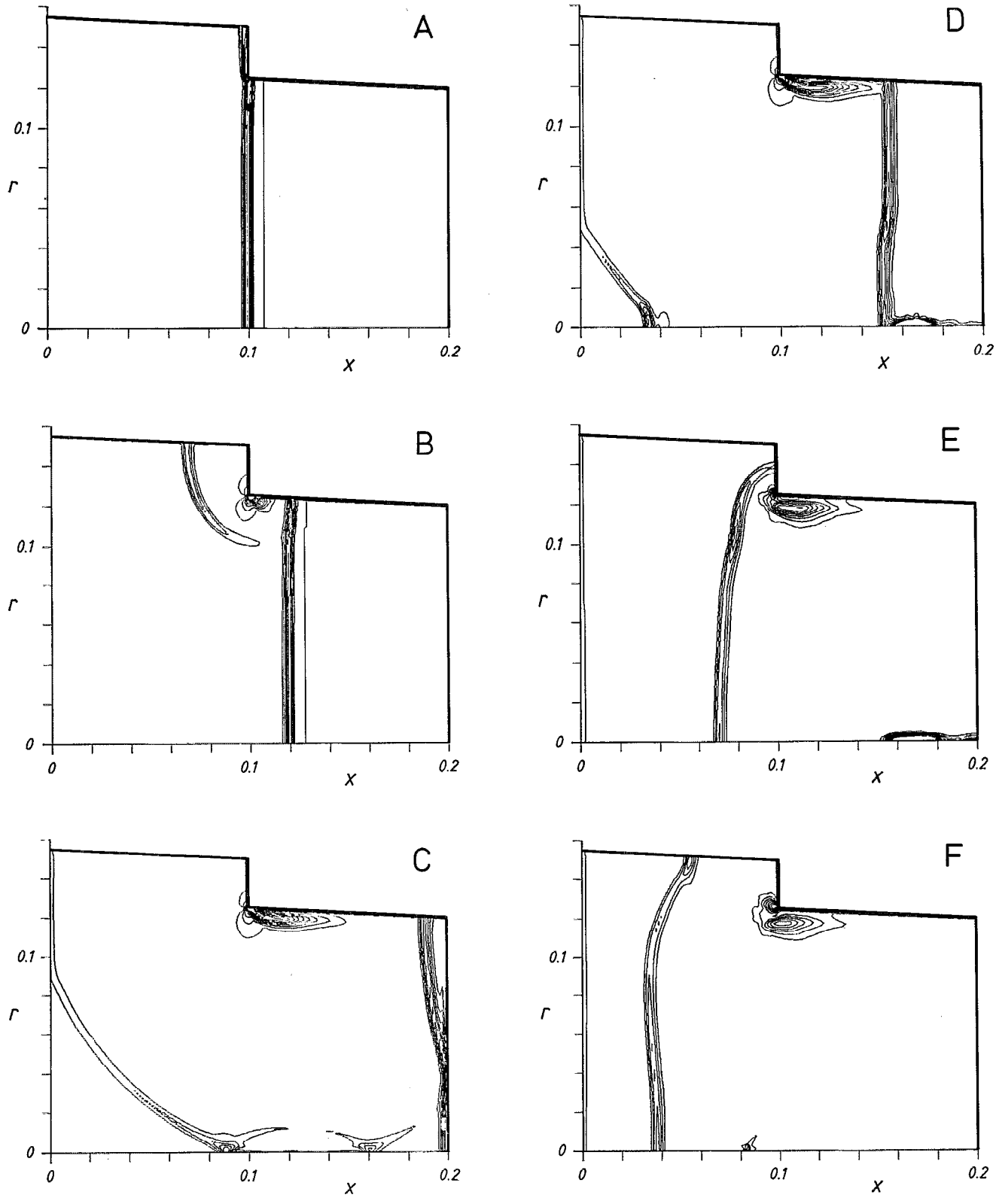

FIG. 6. Time sequence of maximum shear strain rate contours (times as for density). Modified Kawakita equation of state: $A=0.345$, $K=19.778$.

be seen in 4(b) that part of the incident shock is reflected from the die shoulder as a weaker curved shock leaving behind a region of high density above the shoulder. As the main shock is reflected from the end of the die [in 4(c)] it starts to interact with the reflection from the axis of this curved shock and leaves the small area of residual high density seen in the bottom right-hand side of 4(d). This area of high density moves in the negative x direction in Figs. 4(e) and 4(f). Another noticeable feature of Fig. 4 is the region of low density seen in the bottom left-hand cor-

ner of 4(e). These regions of respectively high and low density near the centerline correspond to regions of high and low macrohardness observed in the experimental study. Above the shoulder, also, a zone of high hardness was observed in the experiments corresponding to the high density there originating with the reflection event shown in Fig. 4(b). In powder compacts, macrohardness provides a measure of local density. These results indicate good qualitative agreement between the simulation and experiment on the basis of global density distribution.

2. Vorticity distribution

Figure 5 shows a time frame sequence of vorticity contours in the region of the die shoulder. The azimuthal component of vorticity is defined by

$$\omega \mathbf{k} = \left(\frac{\partial u}{\partial r} - \frac{\partial v}{\partial x} \right) \mathbf{k}, \tag{23}$$

where $\mathbf{k}$ is the unit vector in the azimuthal direction and u and v are the x and r components of velocity, respectively. A concentration of this vorticity can be observed near the corner of the die shoulder at a time 5(a) corresponding to the moment when the incident shock is just starting to pass the shoulder. This vortex, in which the flow is anticlockwise, gradually increases in size up until frame 5(d). As the reflected shock passes the shoulder in the opposite direction in 5(e) a smaller but stronger vortex of opposite sign is formed. Both these vortices become weaker as time goes on [see Fig. 5(f)].

3. Distribution of maximum shear strain rate

Figure 6 shows a time sequence of contours of maximum shear strain rate $\dot{\gamma}_{\max}$. This quantity is calculated by first determining the three principal strain rates,

$$\dot{\epsilon}_1 = \frac{1}{2}\left(\frac{\partial u}{\partial x} + \frac{\partial v}{\partial r} \right) + \left\{ \left[\frac{1}{2}\left(\frac{\partial u}{\partial x} - \frac{\partial v}{\partial r} \right) \right]^2 + \left[\frac{1}{2}\left(\frac{\partial u}{\partial r} + \frac{\partial v}{\partial x} \right) \right]^2 \right\}^{1/2}, \tag{24}$$

$$\dot{\epsilon}_2 = \frac{1}{2}\left(\frac{\partial u}{\partial x} + \frac{\partial v}{\partial r} \right) - \left\{ \left[\frac{1}{2}\left(\frac{\partial u}{\partial x} - \frac{\partial v}{\partial r} \right) \right]^2 + \left[\frac{1}{2}\left(\frac{\partial u}{\partial r} + \frac{\partial v}{\partial x} \right) \right]^2 \right\}^{1/2}, \tag{25}$$

$$\dot{\epsilon}_3 = v/r, \tag{26}$$

and then subtracting the minimum principal strain from the maximum principle strain, i.e.,

$$\dot{\gamma}_{\max} = \max\{\dot{\epsilon}_1, \dot{\epsilon}_2, \dot{\epsilon}_3\} - \min\{\dot{\epsilon}_1, \dot{\epsilon}_2, \dot{\epsilon}_3\}. \tag{27}$$

It can be seen that the regions of high maximum shear strain rate, as indicated by the closely spaced contours, correspond to the location of shock waves (Fig. 4) or vortices (Fig. 5). Importantly, they correspond to the zone of lowest macrohardness, and hence local density, in the previous experiments with this powder.

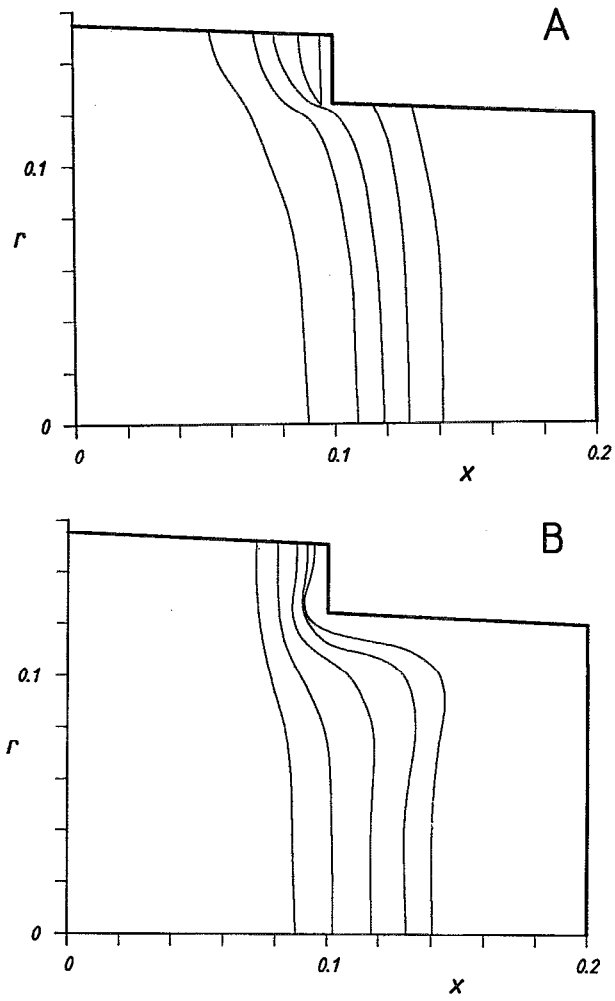

FIG. 7. Comparisons between (a) experimental and (b) EFM particle layer displacements for iron.

4. Material displacement

A simple Euler integration of the motion of points in the marker layers through the calculated velocity field was used in an attempt to simulate the motion of these powder layers. As the layers of marker powder in the experiments were equispaced and outside the die before compaction they reached the die proper at different times. To account for this, the Euler integration used to follow the positions of points in these layers used different starting times depending on the layer.

The EFM simulation was performed for the aluminum, iron, and copper powders using the same number and spacing of marker powder layers as used by Page and Killen. The incident shock Mach numbers were 2.0 for iron, 2.59 for aluminum, and 2.23 for copper. A 40×29 grid size was used and each marker layer was represented by 200 points. Lines were drawn through the final positions of the points and these are compared with the experimental results for iron, copper, and aluminum in Figs. 7, 8, and 9, respectively.

A notable common feature of the experimental and theoretical results for iron, shown in Fig. 7, is the higher-

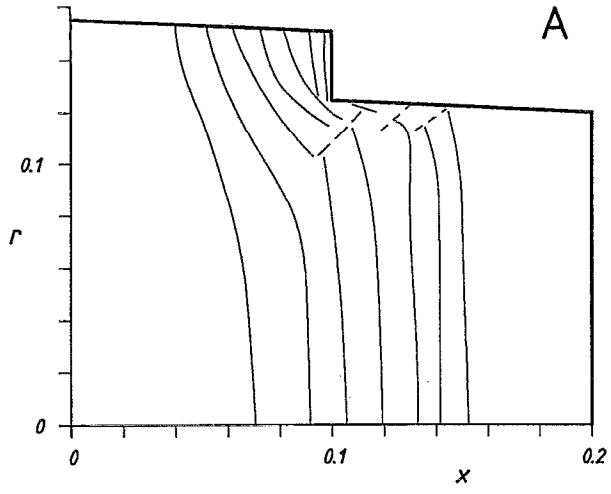

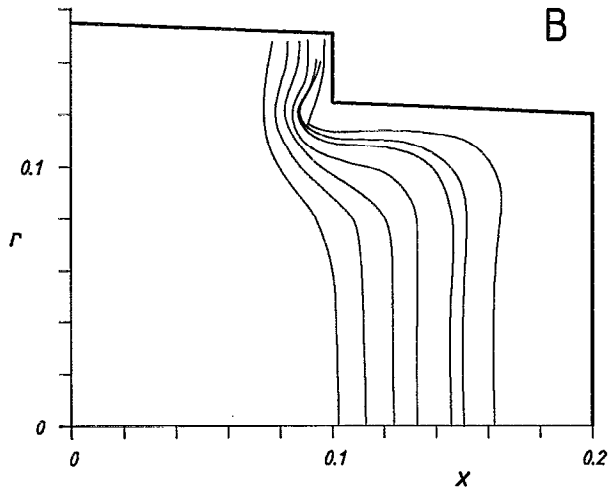

FIG. 8. Comparisons between (a) experimental and (b) EFM particle layer displacements for copper.

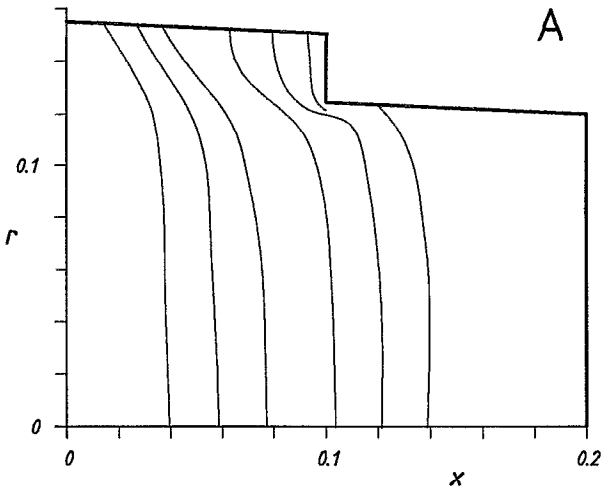

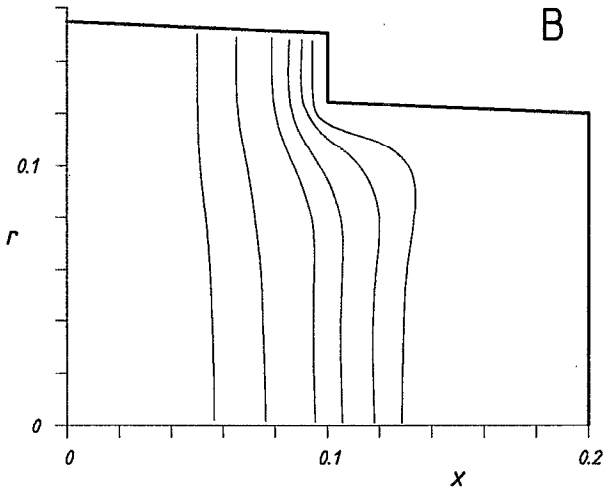

FIG. 9. Comparisons between (a) experimental and (b) EFM particle layer displacements for aluminum.

density region, indicated by the more closely positioned particle layers, just above the die shoulder. However, several differences between the two plots are apparent. The most obvious of these is that the discontinuities in the particle layers in the experimental results are not reproduced in the calculations. This is because the discontinuities are a result of relative motion between different parts of the solid compact, a phenomena that cannot be simulated using fluid flow analogies. Another discrepancy is that in the calculated results the flow near the die wall has not been retarded to the extent that is has been in the experiment. This is because the fluid was assumed to be inviscid and a slip boundary condition is applied at the wall so that no boundary layers that can cause flow retardation can be formed. It is shown in Amin[15] that die-wall friction is affected by several parameters including the load on the powder, particle size, and surface roughness of the die wall. Variables such as particle size and roughness of the die wall are difficult to incorporate into a fluid model.

Examination of Fig. 8 reveals major discontinuities in nearly all the particle layers for copper. Clearly significant relative motion between different portions of the compact along shear surfaces has occurred. This is particularly pronounced in the region below the shoulder. This behavior is most likely a consequence of the very high-strain hardening exponent for copper. As the copper powder flows during compaction it work hardens and becomes more brittle leading to a transition from ductile to brittle deformation behavior. Aluminum, on the other hand, has a low-strain hardening exponent and more closely approximates an elastic perfect plastic material. Thus, as shown in Fig. 9, only smooth flow was observed in the earlier experiments with no evidence of shear surfaces. In this case the only major difference between the experimental and theoretical plots is due to die-wall friction unaccounted for in the EFM model.

The plots shown in Figs. 7–9 demonstrate the main limitations of the inviscid fluid flow assumption: (i) inability to model die-wall friction, and (ii) difficulty in simulating macroscopic solid effects such as discrete shear surfaces. Nevertheless, there is good qualitative agreement between experimental and EFM results with the best agreement being for the material studied that had the lowest work hardening exponent and thus most closely approximated elastic perfect plastic yield behavior.

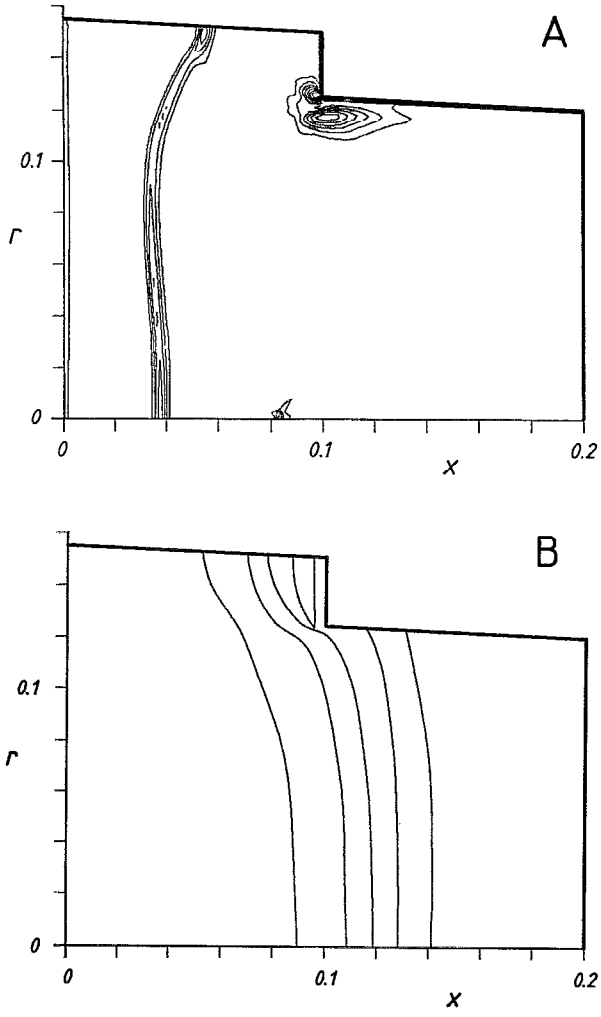

FIG. 10. Comparisons between contour plot of (a) maximum shear strain rate and (b) EFM particle layer displacements for iron.

In Fig. 10 a contour plot of maximum shear strain rate at $t=0.112$ is compared with the experimental particle layer displacements for iron. It can be seen that the region of high shear strain rate near the die shoulder corresponds to a region of bulk relative motion along slip planes in the experimental compact. This, together with the previously discussed correlation between high shear strain rate and low hardness, suggests that a plot of maximum shear strain rate can be used to predict the approximate locations of zones of this relative motion and hence possible regions of weakness in a compacted material.

IV. CONCLUSIONS

From this work it can be concluded that the use of fluid equations to model powder flow, although still in need of further refinement, shows promise. The fluid model was able to predict some of the properties of the final compact such as the high-density region above the die shoulder and high- and low-density regions within the compact. Regions where discrete shear surfaces are likely to occur and local density is likely to be low have been related to regions of high maximum shear strain rate, although quantitative prediction of these effects could not be achieved.

The hydrodynamic fluid flow assumption, despite its limited physical basis, appears to be a useful means of qualitatively predicting many of the properties of the compacted material provided an appropriate equation of state is used.

Further improvements to the results contained herein might be obtained by incorporating viscosity into the model and implementing a boundary condition that accounts for the friction between the die wall and the powder.

ACKNOWLEDGMENT

We gratefully acknowledge support provided by the Australian Research Council under Grant No. A48715757.

[1] D. Raybould, in Proceedings of the 15th International Conference on Machine Tool Design and Research, edited by S. A. Tobias and F. Koenigsberger (MacMillan, London, 1975), p. 627.
[2] H. N. Gourdin, Prog. Mater. Sci. **30**, 39 (1986).
[3] Y. Morimoto, T. Hayashi, and T. Takei, Int. J. Powder Metall. Powder Technol. **18**, 129 (1982).
[4] R. A. Berry and R. L. Williamson, *Metallurgical Applications of Shock Wave and High Strain Rate Phenomena* (Marcel Dekker, New York, 1986), p. 167.
[5] D. I. Pullin, J. Comput. Phys. **34**, 231 (1980).
[6] C. E. Anderson, Int. J. Impact Eng. **5**, 33 (1987).
[7] M. W. Petrie and N. W. Page, J. Appl. Phys. **69**, 3517 (1991).
[8] N. W. Page and D. Raybould, Mater. Sci. Eng. A **118**, 179 (1989).
[9] K. Kawakita and K.-H. Lüdde, Powder Technol. **4**, 61 (1970).
[10] N. W. Page and M. K. Warpenius, Powder Technol. **61**, 87 (1990).
[11] N. W. Page and P. D. Killen, Powder Metal. **30**, 233 (1987).
[12] G. A. Bird, *Molecular Gas Dynamics* (Oxford University Press, Oxford, 1976).
[13] M. N. Macrossan and D. I. Pullin, in Proceedings of the 3rd Australian Supercomputer Conference, University of Melbourne, 1990.
[14] B. Van Leer, J. Comput. Phys. **32**, 101 (1979).
[15] K. E. Amin, Int. J. Powder Metall. **23**, 83 (1987).